

The westward drift of Jupiter's polar cyclones explained by a center-of-mass approach

Nimrod Gavriel^{1*} and Yohai Kaspi¹

¹*Department of Earth and Planetary Sciences, Weizmann Institute of Science, Rehovot, Israel*
**nimrod.gavriel@weizmann.ac.il*

Preprint September 10, 2023

Geophys. Res. Lett., 50, 19, (2023). DOI:[10.1029/2023GL103635](https://doi.org/10.1029/2023GL103635)

(Received Mars 10, 2023; Revised July 18, 2023; Accepted August 29, 2023)

Abstract

The first orbits around Jupiter of the Juno spacecraft in 2016 revealed a symmetric structure of multiple cyclones that remained stable over the next five years. Trajectories of individual cyclones indicated a consistent westward circumpolar motion around both poles. In this paper, we propose an explanation for this tendency using the concept of beta-drift and a "center-of-mass" approach. We suggest that the motion of these cyclones as a group can be represented by an equivalent sole cyclone, which is continuously pushed by beta-drift poleward and westward, embodying the westward motion of the individual cyclones. We support our hypothesis with 2D model simulations and observational evidence, demonstrating this mechanism for the westward drift. This study joins consistently with previous studies that revealed how aspects of these cyclones result from vorticity-gradient forces, shedding light on the physical nature of Jupiter's polar cyclones.

arXiv:2311.11917v1 [astro-ph.EP] 20 Nov 2023

Plain Language Summary

The Juno spacecraft arrived at Jupiter in 2016, revealing a unique atmospheric phenomenon. Each of the poles of Jupiter is inhabited by a symmetrically structured group of cyclones, where a ring of cyclones surrounds one cyclone close to the pole. The collective observations of these cyclones over five years show that although they are relatively stable, they generally drift in the westward direction a few degrees per year. Here, we investigate the mechanism driving this drift by examining the cyclones as a group. This "center-of-mass" approach masks the interactions between the cyclones and only considers trends that happen simultaneously on all cyclones. Using model simulations, we show that the motion of a group's "center of mass" can be captured by a sole equivalent cyclone, pushed poleward and westward by the "beta-drift" effect, which is known to contribute to the motion of tropical cyclones on Earth. This westward force on the group as a whole is thus suggested as the driver of the observed westward drift. We conclude by presenting observational evidence supporting this hypothesis.

Key Points:

- The mean westward circumpolar motion of Jupiter's northern and southern polar cyclones is analyzed and explained by the β -drift effect
- Simulations show that the "center of mass" of a group of cyclones behaves like one equivalent cyclone, moving poleward-westward under β -drift
- This center-of-mass approach is applied to the Juno data, implying that the cyclones' collective β -drift drives their observed westward drift

1 Introduction

The polar cyclones of Jupiter, revealed in 2017 by the Juno mission^{3,4,5}, are comprised of a single polar cyclone (PC) situated near each pole, and multiple circumpolar cyclones (CPCs), 5 at the south pole and 8 at the north pole. The CPCs surround each PC in a ring at approximately latitude $\pm 84^\circ$ (Fig. 1). While the cyclones were observed to retain a stable structure during the five years of measurements, slow motions about their mean positions, and a general westward trend were reported for both poles (Fig. 1; References^{6,7,2,1}). The individual cyclones maintain maximum winds of up to $\sim 100 \text{ ms}^{-1}$ at $\sim 1,000 \text{ km}$ from their cores, and extend to diameters about $5,000 \text{ km}$ ^{8,6}. While a stable configuration of CPCs were never observed before Juno's polar approaches, a polar cyclone has been persistently observed at each pole of Saturn⁹. The formation of a polar cyclone on a gas giant is well understood and revolves around the concept of "beta-drift", which drives cyclonic vortices poleward^{10,11,12,13}, where they converge and maintain a polar cyclone^{14,15,16,17,18}. This β -drift mechanism will be further explained in the following sections.

Given this polar attraction of cyclones, an additional mechanism is needed for explaining the existence of the stable Jovian CPCs, so that they would not merge at the poles. The gradient of planetary vorticity, β , is the driver of β -drift. It was shown that if, in addition to β , the vorticity gradient of the PCs is accounted for when considering β -drift, then the Jovian CPCs are located at a latitude (approximately $\pm 84^\circ$) where the net vorticity gradient vanishes, and thus the CPCs are in a stable equilibrium¹⁹. On Saturn, which is dynamically similar to Jupiter^{20,21,22}, such equilibrium is currently unattainable, inhibiting stable CPCs¹⁹. For the PCs to have a vorticity gradient with the right direction to oppose β , they need to possess an anticyclonic "shielding" around them, as was shown using Shallow-Water (SW) simulations²³.

Observed motion of Jupiter's polar cyclones

In Fig. 1e-f, the reported locations of Jupiter's polar cyclones¹ during the period 2017-2022 are presented. As direct observations of the north polar cyclones were much less frequent than those of the south, the trajectories of the north cyclones are much less constrained. Focusing on the better determined trajectories at the south pole (Fig. 1e), two trends become apparent. One motion trend is a mostly circular motion with a period of ~ 12 months and a radius of $\sim 400 \text{ km}$ ²⁴. This motion was shown to follow a strong correlation between the instantaneous acceleration of each cyclone to the estimated total vorticity gradient under which it moves, suggesting that this motion is driven by the generalized β -drift mechanism²⁴. The second motion trend is an overall westward tendency of each cyclone (Blue arrows in Fig. 1e-f), averaging to about 3° longitude per year at the north pole and 7° at the south¹. In this study, we provide an explanation for this westward trend by considering the generalized β -drift of all the polar cyclones at large. In the following section we explain how one cyclone in a β -plane would feel an acceleration poleward and westward due to β -drift. Then we suggest a "center-of-mass" (CM) approach where the aggregate motion of a group of cyclones can be estimated by the motion of one "equivalent cyclone" following the group's CM, which allows filtering the noisy interactions between the cyclones. Thus, the equivalent cyclone, orbiting the pole due to the poleward component of β -drift would also precess westward due to the westward component of β -drift, projecting on the westward motion of the individual cyclones. We conclude our analysis with observational support for this hypothesis.

2 The evolution of poleward-westward acceleration of barotropic cyclones with a background vorticity gradient

To understand how β -drift can cause the observed westward motion of Jupiter's polar cyclones, we start by reexamining the ideal case of a 2D (barotropic) cyclone under a linear change

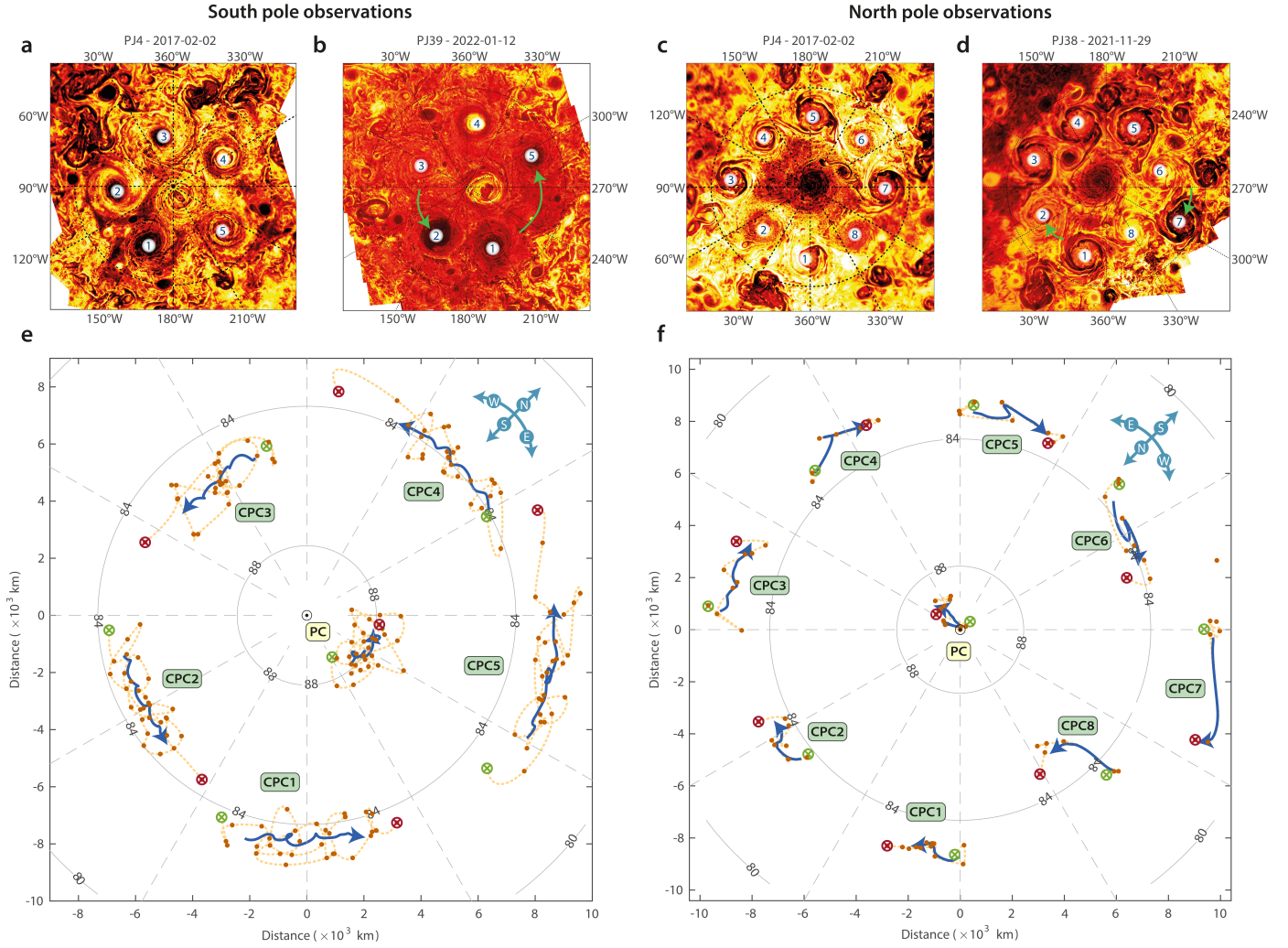


Figure 1: Observations of a westward drift in the north and south poles of Jupiter. (a-d) Infrared images of Jupiter’s poles taken by the Jovian Infrared Auroral Mapper (JIRAM) instrument onboard Juno. These panels were adapted from Ref.¹. (a and b) Images from the south pole in February 2017 (panel a), and in January 2022 (panel b). (c and d) Images from the north pole in February 2017 (panel c), and in November 2021 (panel d). (e and f) Trajectories of the cyclones in the south (panel e) and north (panel f) poles, as observed along 5 years. The orange dots represent the observed locations during Juno’s polar approaches^{2,1}. The dashed yellow curves represent an interpolation of the trajectories between observations. The green and red crosses represent the observed locations in February 2017 and five years later, respectively. The blue arrows represent a moving average of the interpolated trajectories, showing the overall westward trend experienced by the individual cyclones. The gray circles denote the 88°, 84° and 80° latitude lines. The gray dashed lines represent increments of 30° longitude. The point (0,0) represents the pole.

in background vorticity (β -plane). This scenario has been studied extensively in the past in the context of tropical cyclones on Earth, establishing the concept of β -drift, which is the generation of a dipole of vorticity (termed β -gyres) propelling cyclones in a tilted direction relative to the gradient of background vorticity^{10,11,12,13,25,26}. Here, we illustrate the generation of the β -gyres by simulating, using the Dedalus solver²⁷, the secondary vorticity tendency according to the partitioning suggested

by Ref.²⁵. The scaled equation we solve is, at leading order,

$$\frac{\partial \xi_g}{\partial t} = -\hat{\beta} v_v - \mathbf{u}_v \cdot \nabla \xi_g, \quad (1)$$

where ξ_g is the secondary (generated) relative vorticity, and \mathbf{u}_v is a prescribed idealized vortex velocity vector with components (u_v, v_v) in the (x, y) directions, in a grid moving such that the vortex is always at the center (see SI for the full equations and other model details; the used scale factors are supplied in Eq. S6). The first term on the RHS, the advection of background potential vorticity by the vortex (originating from

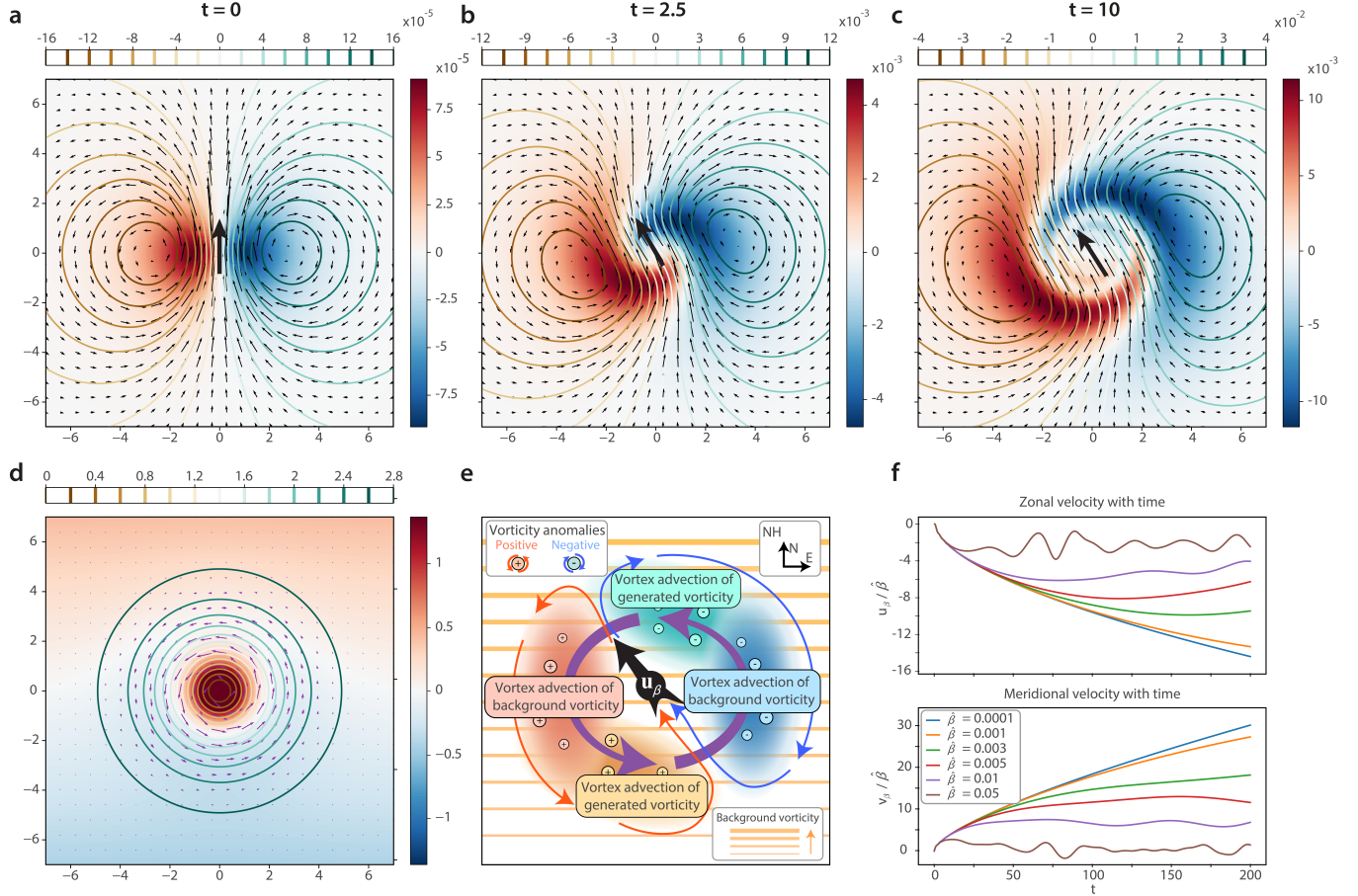


Figure 2: The mechanism for the westward component of β -drift. (a-c) Three snapshots from a simulation showing the development of a β -drift secondary circulation. The red-blue contours represent the generated vorticity. The brown-teal contours are streamlines. Black arrows represent the direction and relative magnitude of the generated velocity field, where the big central arrow represents the instantaneous β -drift advective velocity, at which the cyclone is traveling. All the numbers are unit-less, normalized by the respective cyclone characteristic parameters. (d) The same as panels a-c, but for the primary cyclone circulation forcing the simulation. The north-south color gradient represents the gradient of background vorticity (for illustrative purposes, this gradient is enhanced relative to the values used in the simulation). A video of the simulation is available in SI movie 1. (e) An illustration of the two main terms ($\times 2$ for each side) that determine β -drift, according to Eq. 1. The purple arrow represents the cyclone's tangential velocity (\mathbf{u}_v). The orange lines represent the background vorticity, where thicker lines represent larger magnitudes. The red-orange (blue-turquoise) clouds with plus (minus) signs represent generation of positive (negative) vorticity. The red (blue) arrows represent the generated cyclonic (anti-cyclonic) secondary circulation. The black arrow is the resulting β -drift velocity. While this illustration is for the northern hemisphere, the same principles work for the southern hemisphere, where a poleward-westward drift is generated as well (see the equivalent Fig. S1). (f) Time evolution of the simulated β -drift velocity at the center of the cyclone, divided by $\hat{\beta}$ (black arrow in the center of panels a-c). Different colors represent different $\hat{\beta}$ values, showing that for a significant period of the acceleration, the velocities are proportional to $\hat{\beta}$.

the curl of the Coriolis force), is proportional to the unit-less parameter $\hat{\beta} = \Delta f / \omega$, which is the ratio between the change in background vorticity across the core of the vortex ($\Delta f = \beta R$, where R is the radius of maximum velocity in the vortex), and the rotation frequency scale of the vortex ($\omega = V/R$, where V is the maximum velocity in the vortex). Thus, this parameter en-

capsulates how steep is the vorticity gradient across the cyclone, which in turn would determine the resulting magnitudes of ξ_g . In addition, the second term on the RHS of Eq. 1 represents the subsequent advection of generated ξ_g by the primary circulation of the vortex. The full solved equation also contains the nonlinear terms, a numerical viscosity term and a sponge term which

helps avoid effects from the double periodic boundaries.

In Fig. 2a-c, three simulation snapshots are plotted for ξ_g , resulting from the primary vortex circulation in a β -plane, as shown in Fig. 2d. As the simulation begins from rest ($\xi_g = 0$), the only term generating vorticity immediately after $t = 0$ (Fig. 2a) is the $-\hat{\beta}v_v$ term, which changes according to the meridional velocity of the primary circulation. As such, near $t = 0$, we have a dipole oriented in the x direction, creating an initial acceleration northward (towards the gradient of background vorticity). This ξ_g generation is illustrated as the red and blue regions in Fig. 2e, representing the advective flux of background vorticity by \mathbf{u}_v . Then, this generated ξ_g dipole is twisted by \mathbf{u}_v (Fig. 2b-c and orange and turquoise clouds in Fig. 2e), accelerating the vortex in the westward direction. The direction of the β -drift velocity vector (\mathbf{u}_β) is determined by the diagonal line where the terms $-\hat{\beta}v_v$ and $-\mathbf{u}_v \cdot \nabla \xi_g$ cancel each other. This direction is poleward-westward for cyclones with background vorticity increasing poleward, but would flip to equatorward-eastward if the background vorticity increases equatorward (Fig. S1), such as in the case when the Jovian CPCs get too close to the shielded PCs^{19,24}.

An account of the acceleration of β -drift with time can be seen in Fig. 2f, showing how the secondary velocities at the center of the cyclone (u_β and v_β in the x, y directions, respectively) are proportional to $\hat{\beta}$ for the majority of the acceleration phase. If the velocities were not scaled by $\hat{\beta}$, the different curves would have magnitudes proportional to $\hat{\beta}$, but this scaling fuses the curves together. The curves eventually separate due to the accumulation of non-linearities. This separation happens sooner for simulations with larger $\hat{\beta}$. The direction of \mathbf{u}_β can be calculated from the two panels of Fig. 2f as $\tan^{-1}(v_\beta/u_\beta)$. The time is scaled by R/v , which is of order ~ 3 hours for Jupiter's cyclones; the velocity is scaled by V , in addition to $\hat{\beta}$. It can be seen that the model is unstable for $\hat{\beta}$ values on the order of 5×10^{-2} and larger, which we assume to be due to the non-linear effects. The $\hat{\beta}$ values of Jupiter's polar cyclones are between 10^{-4} to 10^{-3} (Fig. 4), and thus are represented well by the linear solutions. Another thing to note here about the applicability of Fig. 4f to the Jovian polar cyclones is that as the cyclones move around, the effective β under which they operate changes its magnitude and direction, resulting in a resetting (or partial resetting) of the β -drift phase seen in Fig. 4f and limiting the late-time evolution of the β -drift.

3 The center of mass for a group of cyclones and the motion of an equivalent cyclone

In previous numerical studies of tropical cyclones, it was shown that two identical cyclones on an f -plane may orbit each other due to their mutual interaction, but once a poleward background vorticity gradient (β) is introduced, both cyclones gain a poleward-westward motion, while their motion relative to one another

stays the same as in the f -plane scenario²⁸. Thus, it can be inferred that an equivalent cyclone positioned in the CM of the cyclones, moves according to β -drift while absorbing the mutual interactions. To test this idea further, we use Dedalus to solve the barotropic vorticity equation, this time without the partitioning to primary and secondary circulations as in Fig. 2, so that

$$\frac{D\xi}{Dt} = -\beta v, \quad (2)$$

where $D/Dt = (\partial/\partial t + \mathbf{u} \cdot \nabla)$ is the material derivative, \mathbf{u} is the velocity vector (with components u and v in the x and y directions, respectively) and $\xi = \nabla \times \mathbf{u}$ is relative vorticity. Similar to the model in the previous section, here also a numerical viscosity term and a trap term (analogous to the one used in Ref. ²⁹), are added to the model.

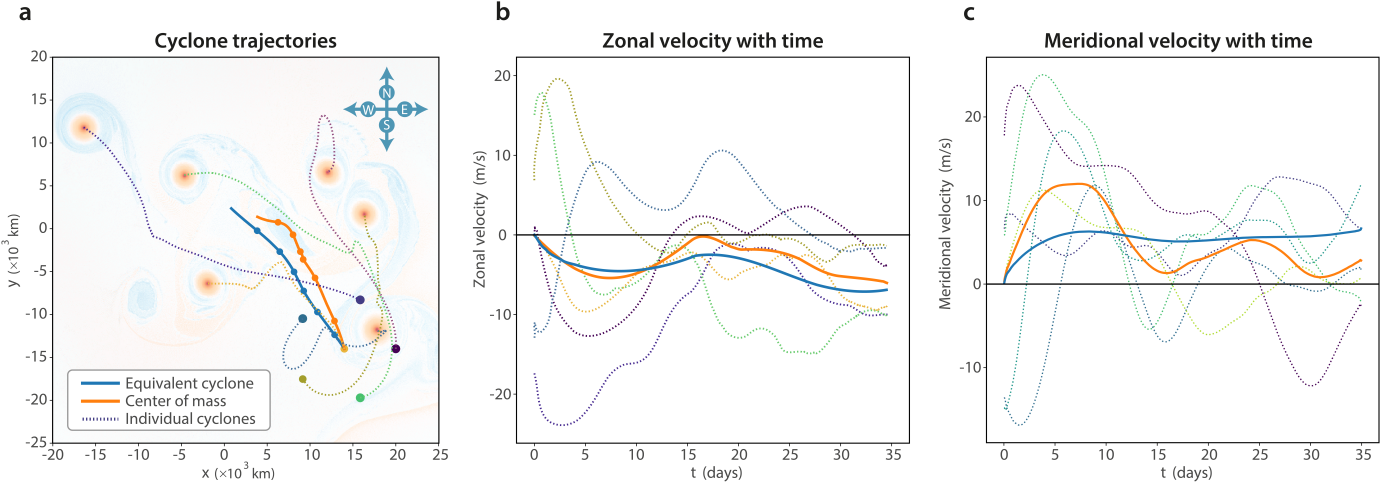
Eq. 2 is integrated on a β -plane from an initial condition of a group of 6 identical cyclones positioned according to the colored dots in Fig. 3a (see full model specifications in the SI). The dashed curves are the Cartesian trajectories of the 6 cyclones and the orange curve represents the motion of their CM, calculated as the arithmetic mean of the instantaneous positions of the cyclones. In addition, another simulation is presented where only one equivalent cyclone, identical to the cyclones in the group, begins its motion from the center of the group and follows almost the exact trajectory of the CM. Thus, the motion is decoupled to two contributions, one is the north-westward motion of each cyclone due to β -drift, taking only β into account, and the other is the mutual interactions between the cyclones, which are absorbed when following the CM. The slight difference between the trajectories of the CM and the equivalent cyclone likely owes to non-linearities. To evaluate how should the cyclones be weighted in order to determine the CM when cyclones are not identical, we derive a weight estimation (see derivation in the SI) based on integrated vorticity gradient forces between two cyclones (Fig. S2), leading to

$$W_i = \frac{e^{-\frac{L}{R_i}} R_i^{-4}}{\sum \left(e^{-\frac{L}{R_j}} R_j^{-4} \right)}, \quad (3)$$

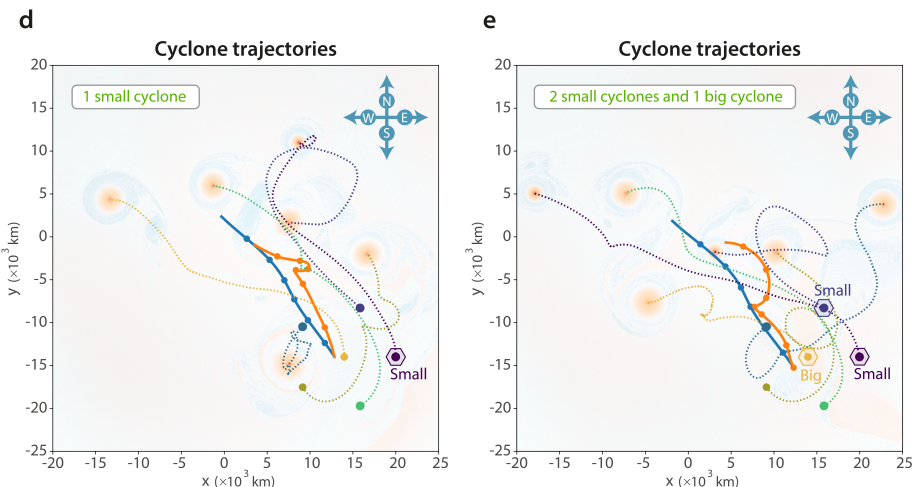
where W is relative weight, i (or j) is the cyclone's index, L is an average distance between the cyclones and the sum is over all the cyclones in the group. With this weight estimation, two other test cases are performed (Fig. 3d-e), similar to Fig. 3a-c, but where the cyclones vary in their sizes, leading to similar results.

The implication of this idealized case to Jupiter's polar cyclones is non-trivial due to, e.g., variations in the cyclones' properties within the group and the non-linear background vorticity (which behaves like a cosine of latitude). Our hypothesis is thus (Fig. 3f), that if we look on an equivalent cyclone in the polar case, this cyclone only feels the acceleration due to β -drift, with no dependence on the inter-cyclone interactions. This means that while a CPC would feel alternating poleward-westward and equatorward-eastward accelerations by β and by interactions with the vorticity gradient of the other cyclones²⁴,

6 Identical cyclones on a β -plane



Cases with size variance



The mechanism for the westward drift

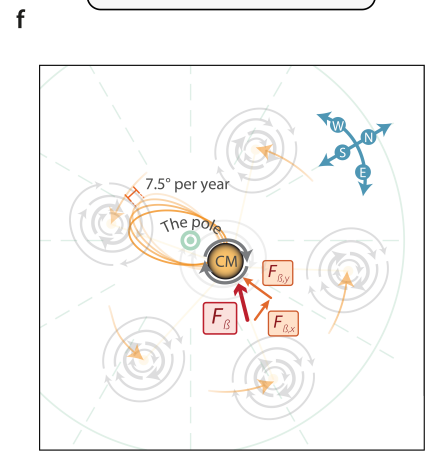


Figure 3: A CM approach for a group of cyclones. (a-e) The simulated motion of 6 cyclones on a β -plane and of their equivalent cyclone. (a) The Cartesian trajectories with time. The colored dots are the initial locations of 6 identical cyclones. The colored dotted lines are the trajectories of the individual cyclones. The orange (blue) curve represents the trajectory of the CM (equivalent cyclone), where the dots represent constant time intervals. The red-blue contour represent the relative vorticity map at the final snapshot. The colors are enhanced for illustrative purposes. (b and c) The same as panel a, but here the abscissa is time and the ordinate is zonal and meridional velocity, respectively. (d) The same as panel a, but in this case one of the cyclones is smaller by 50%. (e) Another simulation, similar to panel a, where two cyclones are smaller by 50%, and one cyclone is larger by 20%. See SI Movie 2 for a video of the entire simulation of the 6 cyclones and SI Movie 3 for a video of the equivalent cyclone simulation (for the case with identical cyclones). (f) An illustration of how the poleward-westward β -drift acceleration can create a net westward drift in Jupiter's poles when looking from the perspective of a CM. The transparent cyclones represent the CPCs. The red arrow is the β -drift acceleration, where the orange arrows are the meridional and zonal components. The orange ellipses illustrate the motion of the CM around the pole, where the ellipse precesses westward due to the zonal component of the β -drift.

on average, the residual is only due to β . The poleward component of the β -drift on the CM's equivalent cyclone would then maintain an elliptical orbit around the pole, and the westward component would rotate this orbit in the zonal direction. It is therefore proposed that the projection back to the cyclones of this rotation is the mechanism behind the observed westward drift at Jupiter's poles. In the following section we use Juno's observations to support this hypothesis.

4 The center of mass of the polar cyclones in the observations.

The most straightforward way to calculate the CM is by taking the arithmetic mean of the locations of all the polar cyclones (the Cartesian projected locations, (x, y) ; see Eq. S1). To take into account the different sizes of the cyclones, which were previously estimated from Juno's observations⁶, we use Eq. 3 for a weighted average of the Cartesian coordinates when determining the CM's trajectory along the period of the observations (See SI for the calculation procedure and the used values). As the data from the north pole is too infrequent, we only use the data from the south pole for Fig. 4a-e (Ref.¹, see Fig. S3 for the equivalent north-pole figure, based on the existing observations). It can be seen (Fig. 4a) that the CM's trajectory is indeed very clean, and possesses mostly the 12-month oscillations exhibited by the individual cyclones (Fig. 4d-e, Ref.²⁴). This suggests that this 12-month mode of motion is mostly synchronized between the cyclones, and is therefore largely due to the motion of the CM (i.e., the first mode of motion where all cyclones oscillate together as a group). In both the zonal and meridional cases, short-period modes are suppressed for the CM (Fig. 4d-e). When considering an elliptical orbit with a radial force in the direction of the pole (Fig. 3f), the ellipse is expected to have its semi-major axis in the meridional direction. Consistently, the 12-month amplitude of the CM is larger in the meridional direction than in the zonal (Fig. 4d-e).

One conflict between the hypothesis (Fig. 3f) and the CM measurement (Fig. 4a) is that the measured CM trajectory does not encompass the pole. This might be due to errors in estimating the weights of the cyclones (e.g., measurement errors, sparsity of data, and approximations in deriving Eq. 3), which may also change in time during the observation period for the real cyclones. To test the sensitivity of the results (Fig. 4) to the prescribed weights and the factor L (Eq. 3), an analysis of randomly generated cyclone sizes is concluded, showing that the observation-based sizes significantly improve the results when comparing equivalent analyses with random or with identically sized cyclones (Fig. S4). Also, investigating the role of the parameter L (Fig. S5), we find that the used value of 6,000 km, representing an observationally based average distance between the cyclones (see Fig. 1e-f), gives the best results in terms of how close is the CM's motion to encompassing the pole.

The time-series of the CM's motion (Fig. 4b) indeed appears to have a clean sinusoidal form, where the inter-cyclone interac-

tions of the individual cyclones (Fig. 4c) are filtered. The linear fit for the CM's longitude with time (Fig. 4b) has a slope of 8.17° longitude per year. The analogous linear fits for the individual cyclones (Fig. 4c) have slopes of $8.23 \pm 0.71^\circ$ longitude per year, suggesting that indeed the zonal drift of the cyclones is a projection of the CM's zonal drift (see the lower panel of Fig. 4f for all values, including the north pole). Two reported incidents where an "intruder" vortex appeared in the south polar ring (PJ 18 & 23, References^{6,2}) are marked (purple vertical lines in Fig. 4b-c) as a possible explanation for the perturbations in the sinusoidal motion of the CM proximate to these observations.

Finally, the results from Figs. 1-4 are tied together in Fig. 4f. Here, the values of $\hat{\beta}$ for the cyclones and for the CM are estimated. As the effective β for the individual cyclones is close to zero, representing perturbations near stable equilibrium, the values of β (for estimating $\hat{\beta}_i$ of each cyclone i) are set equal for all of the cyclones and for the CM at each pole, and are determined by a vector sum of the β each cyclone is subject to (see SI). It can be seen (Fig. 4f) that indeed $\hat{\beta}$ of the CMs in the north and south poles are proportional to their respective zonal motion. Here we calculate the CM motion using two different methods (See SI for the detailed calculations). For CM1, the velocities are the weighted (according to Eq. 3) average of the individual cyclones' zonal velocities. For CM2, the velocities are calculated by a linear fit of the instantaneous zonal displacements of the CM. Using Fig. 2f with the values of $\hat{\beta} \approx 7 \times 10^{-4}$, we get an overestimation in the scale of the zonal velocities of an order of magnitude relative to the south pole values in the upper panel of Fig. 4f. Our interpretation of this discrepancy is that the steady state condition may have a form of dissipation which balances the β -drift acceleration at low values of zonal velocities. Another consideration is a relative vorticity turbulent mixing that may reduce the vorticity gradient of one cyclone under another cyclone²⁹ relative to our estimations, which are extrapolated from the profiles at the vicinity of the cyclones. Nevertheless, when using the method CM1 for the metric zonal velocity, which is the more physical form of velocity as related to the β -drift, it can be seen that both $\hat{\beta}$ and the CM's zonal velocity are approximately two times larger in the south pole than in the north pole (dashed line in the upper panel of Fig. 4f). This proportionality is expected to be true regardless of dissipation or turbulent mixing, and provides support to the given hypothesis for the westward drift in Jupiter's poles.

5 Discussion

Since the discovery of Jupiter's polar cyclones, the role of vorticity gradient forces (or generalized β -drift), which takes into account both β and the relative vorticities of all neighboring cyclones, presented a consistent picture. These forces were used to explain the mean latitude of the cyclones and their number¹⁹, the oscillatory motion patterns of the cyclones²⁴, and now their mean westward drifts as well. This series of studies, revealing different aspects of these forces, implies that these po-

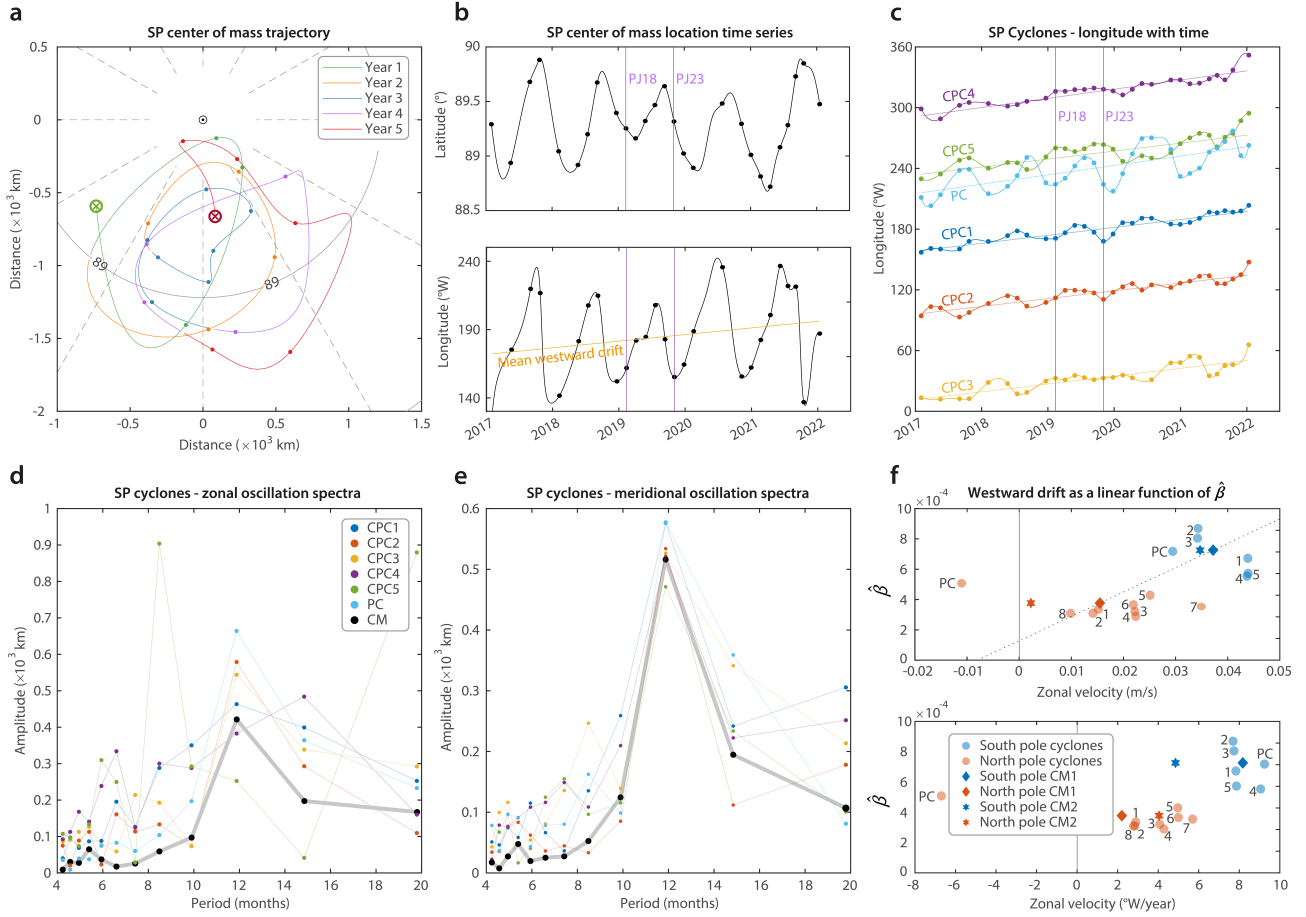


Figure 4: Calculations of the CM from the observations. (a) The Cartesian trajectory of the CM in the south pole of Jupiter according to the cyclone trajectories presented in Fig. 1e (dots and curves represent real data and interpolation, respectively). The curve changes color with the passing of every year to illustrate the 1-year oscillatory motion exhibited in the CM’s motion. (b) The latitude (upper panel) and longitude (lower panel) of the south CM with time. The purple vertical lines represent two incidents of an intruder cyclone during PJs 18 and 23. The orange line represents the linear fit of the westward location of the CM with time. (c) The longitude with time of each of the south polar cyclones. The straight lines represent linear fits for each cyclone, showing the westward motion. (d and e) The zonal and meridional oscillation spectra of the south polar cyclones (color) and of the CM (black). (f) The relation between the measured zonal velocities of the cyclones and $\hat{\beta}$. Zonal velocities are 5-year averages in metric units at the upper panel and longitude ($^{\circ}$ W) per year in the lower panel. Red and blue points represent values for the north and south poles, respectively. The numbers identify the respective CPCs. The diamond and star shapes represent two different approaches for calculating the CM’s zonal velocities as discussed in the text.

lar cyclones behave, to leading order, like discrete objects, linearly forced by a “spring-like” system driving them all in the poleward-westward direction while pushing them one from another. There are many uncertainties in the observations, such as variations between the velocity profile of each cyclone (and how it changes in time³⁰) and the low resolution of the cyclones’ tracks¹, especially in the north pole, in addition to complexities in the conversion of the CM concept from Cartesian to concentric polar coordinates and others.

However, we see that the CM of the cyclones has an organized motion (Fig. 4), filtering the inter-cyclone exchanges as in the idealized case (Fig. 3a-e), and that the relative westward

velocities of the CMs in the north and south poles, representatives of “equivalent” cyclones for the two groups, correlate with their different $\hat{\beta}$, as expected from the idealized cyclone simulations (Fig. 2). These make the case that indeed the cumulative β -drift, integrated over all the cyclones in the group is the mechanism for the observed westward drift of the cyclones. In this regard, we note that the westward drift in itself is surprising, since the PCs, if possessing considerable velocities as far equatorward as the CPCs, would advect the CPCs eastward around both poles. But, seeing that the longitudinal displacements are similar between the CPCs, the PCs and the CMs (lower panel of Fig. 4f), we conclude that advective steering of the CPCs by

the PC winds is unimportant, or is offset by the CM’s westward drift. An important intuition for the contrast between the drift rates of the north and south poles can be derived from the fact that the ring of CPCs at the north pole is much more concentric (to the pole) than at the south pole (Fig. 1). Therefore, the CM at the north is closer to the “rest” position at the pole, leading to a smaller β of the CM and a respectively smaller westward drift, than at the south. Thus, if the cyclones were put such that their CM rests exactly at the pole, no westward drift would be expected.

Another piece of important information that is still missing about these polar cyclones relates to the mechanism driving them and maintaining them against dissipation. In a recent barotropic numerical study, a step was taken in that direction, showing that initial small-scale turbulent conditions can “cool down” to form CPCs around a polar cyclone²⁹. This study is in agreement with observational evidence showing that kinetic energy in the Jovian polar region follows an inverse energy cascade, where energy originating in small-scale turbulence is passed to the large-scale cyclones^{31,32}. Regarding the depth of the cyclones, the β -drift framework, explaining many observations, suggests that the cyclones are deep²⁴. This is in agreement with the small Rossby number near the poles, suggesting the 2D Taylor-Proudman theorem regime^{33,34}. However, there is still a gap towards understanding the mechanisms driving the cyclones, which might reveal what determines their size, strength and form. Finally, the unique conditions in Jupiter’s poles, provided striking opportunity to test, in the physical world, theories derived for explaining the motion of tropical cyclones on Earth^{12,13,28}, where their transient nature and complex environment make the task of diagnosing their motion extremely difficult. These theories prove themselves consistently in Jupiter’s polar cyclones, and assist in constructing the physical picture behind their surprising existence.

Open Research

No new data sets were generated during the current study. The data analyzed in this study were published by Ref.¹ (DOI: <https://doi.org/10.1029/2022JE007241>), as cited in the text. The simulations were run with the Dedalus solver²⁷ (DOI: <https://doi.org/10.1103/PhysRevResearch.2.023068>).

acknowledgments

This research has been supported by the Minerva Foundation with funding from the Federal German Ministry for Education and Research and the Helen Kimmel Center for Planetary Science at the Weizmann Institute of Science. We thank Keren Duer, Eli Galanti, Or Hadas, Rei Chemke and Quentin Nicolas for insightful conversations and helpful feedback.

Competing Interests

Authors declare that they have no competing interests.

References

1. Mura, A. *et al.* Five years of observations of the circumpolar cyclones of Jupiter. *J. Geophys. Res. (Planets)* **127**, e2022JE007241 (2022).
2. Mura, A. *et al.* Oscillations and stability of the Jupiter polar cyclones. *Geophys. Res. Lett.* **48**, e2021GL094235 (2021).
3. Bolton, S. J. *et al.* Jupiter’s interior and deep atmosphere: The initial pole-to-pole passes with the Juno spacecraft. *Science* **356**, 821–825 (2017).
4. Orton, G. S. *et al.* The first close-up images of Jupiter’s polar regions: Results from the Juno mission JunoCam instrument. *Geophys. Res. Lett.* **44**, 4599–4606 (2017).
5. Adriani, A. *et al.* Clusters of cyclones encircling Jupiter’s poles. *Nature* **555**, 216–219 (2018).
6. Adriani, A. *et al.* Two-year observations of the Jupiter polar regions by JIRAM on board Juno. *J. Geophys. Res. (Planets)* e2019JE006098 (2020).
7. Tabataba-Vakili, F. *et al.* Long-term tracking of circumpolar cyclones on Jupiter from polar observations with JunoCam. *Icarus* **335**, 113405 (2020).
8. Grassi, D. *et al.* First estimate of wind fields in the Jupiter polar regions from JIRAM-Juno images. *J. Geophys. Res. (Planets)* **123**, 1511–1524 (2018).
9. Baines, K. H. *et al.* Saturn’s north polar cyclone and hexagon at depth revealed by Cassini/VIMS. *Planet. Space Sci.* **57**, 1671–1681 (2009).
10. Rossby, C. On displacements and intensity changes of atmospheric vortices. *J. Mar. Res.* **7**, 71 (1948).
11. Adem, J. A series solution for the barotropic vorticity equation and its application in the study of atmospheric vortices. *Tellus* **8**, 364–372 (1956).
12. Fiorino, M. & Elsberry, R. L. Some aspects of vortex structure related to tropical cyclone motion. *J. Atmos. Sci.* **46**, 975–990 (1989).
13. Smith, R. K. & Ulrich, W. An analytical theory of tropical cyclone motion using a barotropic model. *J. Atmos. Sci.* **47**, 1973–1986 (1990).
14. Scott, R. Polar accumulation of cyclonic vorticity. *Geophys. Astrophys. Fluid Dyn.* **105**, 409–420 (2011).
15. O’Neill, M. E., Emanuel, K. A. & Flierl, G. R. Polar vortex formation in giant-planet atmospheres due to moist convection. *Nature Geoscience* **8**, 523–526 (2015).
16. O’Neill, M. E., Emanuel, K. A. & Flierl, G. R. Weak jets and strong cyclones: Shallow-water modeling of giant planet polar caps. *J. Atmos. Sci.* **73**, 1841–1855 (2016).
17. Brueshaber, S. R., Sayanagi, K. M. & Dowling, T. E. Dynamical regimes of giant planet polar vortices. *Icarus* **323**, 46–61 (2019).
18. Hyder, A., Lyra, W., Chanover, N., Morales-Juberías, R. & Jackiewicz, J. Exploring Jupiter’s polar deformation lengths with high-resolution shallow water modeling. *Planet. Sci. J.* **3**, 166 (2022).
19. Gavriel, N. & Kaspi, Y. The number and location of

- Jupiter's circumpolar cyclones explained by vorticity dynamics. *Nature Geoscience* **14**, 559–563 (2021).
20. Showman, A. P., Ingersoll, A. P., Achterberg, R. & Kaspi, Y. The global atmospheric circulation of Saturn. *Saturn in the 21st Century* **20**, 295 (2018).
 21. Galanti, E. *et al.* Saturn's deep atmospheric flows revealed by the cassini grand finale gravity measurements. *Geophys. Res. Lett.* **46**, 616–624 (2019).
 22. Kaspi, Y. *et al.* Comparison of the deep atmospheric dynamics of Jupiter and Saturn in light of the Juno and Cassini gravity measurements. *Space Sci. Rev.* **216**, 5, 84, 1–27 (2020).
 23. Li, C., Ingersoll, A. P., Klipfel, A. P. & Brettle, H. Modeling the stability of polygonal patterns of vortices at the poles of Jupiter as revealed by the Juno spacecraft. *Proc. Natl. Acad. Sci. U.S.A.* **117**, 24082–24087 (2020).
 24. Gavriel, N. & Kaspi, Y. The oscillatory motion of Jupiter's polar cyclones results from vorticity dynamics. *Geophys. Res. Lett.* **49**, e2022GL098708 (2022).
 25. Smith, R. K., Ulrich, W. & Dietachmayer, G. A numerical study of tropical cyclone motion using a barotropic model. I: The role of vortex asymmetries. *Q. J. R. Meteorol. Soc.* **116**, 337–362 (1990).
 26. Smith, R. K. & Ulrich, W. Vortex motion in relation to the absolute vorticity gradient of the vortex environment. *Q. J. R. Meteorol. Soc.* **119**, 207–215 (1993).
 27. Burns, K. J., Vasil, G. M., Oishi, J. S., Lecoanet, D. & Brown, B. P. Dedalus: A flexible framework for numerical simulations with spectral methods. *Physical Review Research* **2**, 023068 (2020).
 28. Chan, J. & Law, A. The interaction of binary vortices in a barotropic model. *Meteorol. Atmos. Phys.* **56**, 135–155 (1995).
 29. Siegelman, L., Young, W. R. & Ingersoll, A. P. Polar vortex crystals: Emergence and structure. *Proc. Natl. Acad. Sci. U.S.A.* **119**, e2120486119 (2022).
 30. Scarica, P. *et al.* Stability of the Jupiter southern polar vortices inspected through vorticity using Juno/JIRAM data. *J. Geophys. Res. (Planets)* **127**, e2021JE007159 (2022).
 31. Moriconi, M. *et al.* Turbulence power spectra in regions surrounding Jupiter's south polar cyclones from Juno/JIRAM. *J. Geophys. Res. (Planets)* **125**, e2019JE006096 (2020).
 32. Siegelman, L. *et al.* Moist convection drives an upscale energy transfer at Jovian high latitudes. *Nature Physics* 1–5 (2022).
 33. Busse, F. H. A simple model of convection in the Jovian atmosphere. *Icarus* **29**, 255–260 (1976).
 34. Vallis, G. K. *Atmospheric and oceanic fluid dynamics* (Cambridge University Press, 2017).
 35. Chan, J. C. & Williams, R. Analytical and numerical studies of the beta-effect in tropical cyclone motion. part I: Zero mean flow. *J. Atmos. Sci.* **44**, 1257–1265 (1987).

Supplementary Information

Movie S1. ([Link](#)) A movie showing the development of the β -gyres. This is the full time evolution, from which the three snapshots of Fig. 2 in the main text are taken. The left panel describes the vorticity and the right panel is the stream-function. All variables are scales according to SI section 2.

Movie S2. ([Link](#)) A movie showing the vorticity evolution of the 6 identical cyclones β -plane experiment. The model is described in SI section 3.

Movie S3. ([Link](#)) A movie showing the vorticity evolution of the equivalent cyclone β -plane experiment. The model is described in SI section 3.

A Cyclone paths from the observations

Here we prescribe the methods we used for plotting the trajectories in Fig. 1. For this study we used the data acquired by the JIRAM instrument, as published in Ref. ¹, where the locations of the centers of the polar cyclones in the north and south poles are laid out for Juno perijoves (PJs), where they were located in terms of longitude ($^{\circ}$ W) and latitude ($^{\circ}$ N). The first step in the analysis was to convert these locations to a Cartesian grid according to

$$x = -R_J \cos \theta \sin \lambda, \quad y = R_J \cos \theta \cos \lambda, \quad (4)$$

where R_J is the radius of Jupiter, θ is latitude and λ is longitude. The planetary radius here, calculated as $R_J = (R_e^2/R_p) = 76,452$ km¹⁸, is the osculating radius, taking Jupiter’s oblateness into account. This data, per PJ, is temporally interpolated separately for the x and y coordinates. The blue arrows of Fig. 1e-f are moving averages over the interpolated data, with an averaging window of ~ 1.3 years (endpoints are disposed; i.e., data points 0.65 years from the start or the end are not shown in the moving average).

B Beta-drift simulations

In this section, the model used for producing Fig. 2 is described.

Model equations

We begin with the 2D barotropic vorticity equation,

$$\frac{D}{Dt} (\xi + f) = 0, \quad (5)$$

where

$$\frac{D}{Dt} = \left(\frac{\partial}{\partial t} + \mathbf{u} \cdot \nabla \right) \quad (6)$$

is the material derivative, \mathbf{u} is the velocity vector, $\xi = \nabla \times \mathbf{u}$ is relative vorticity and f is the vertical component of the planetary vorticity, or, in the context of this study, any background vorticity profile. Eq. 5 is then partitioned, as suggested by Ref. smith1990numerical, into two coupled equations. One equation describes the advection of a vortex by β -drift as

$$\frac{\partial \xi_v}{\partial t} + \mathbf{u}_\beta \cdot \xi_v = 0, \quad (7)$$

where $\xi_v = \nabla \times \mathbf{u}_v$ describes the relative vorticity of a symmetric vortex, \mathbf{u}_v is the velocity vector of the vortex, and \mathbf{u}_β is the velocity vector of the β -drift. The second equation is

$$\frac{\partial \xi_g}{\partial t} + (\mathbf{u}_v + \mathbf{u}_g) \cdot \nabla (\xi_g + f) + (\mathbf{u}_g - \mathbf{u}_\beta) \cdot \nabla \xi_v = 0, \quad (8)$$

where $\xi_g = \nabla \times \mathbf{u}_g$ describes the “generated” relative vorticity, and \mathbf{u}_g , the generated velocity vector, describes the generation of vorticity anomalies (relative to the symmetric vortex) by the advection of net vorticity, in a grid moving with \mathbf{u}_β . The term $\mathbf{u}_v \cdot \nabla \xi_v$ was eliminated for Eq. 8 as this prescribed vortex flow is symmetric around the vortex and flows along lines of equal ξ_v . In this

Beta drift directions for cyclonic vortex under background vorticity gradient

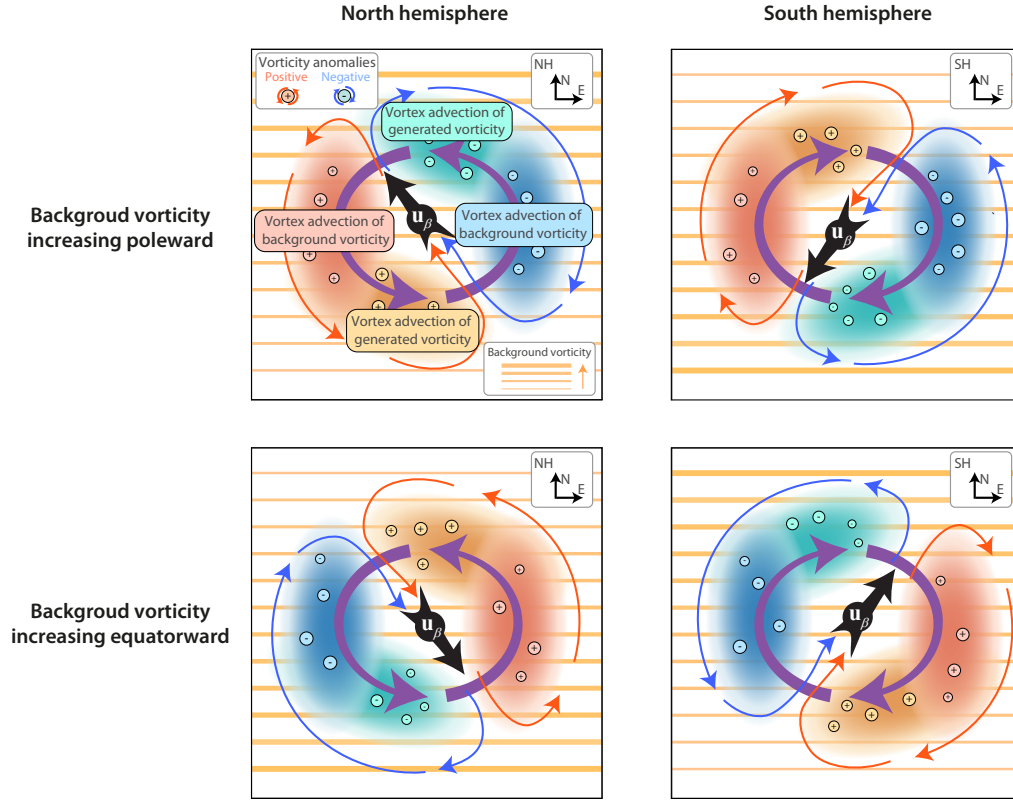


Figure S1: Generalization of Fig. 2e of the main text. Here the upper left panel is the same as Fig. 2e. The left column represents β -drift of a cyclonic vortex in the north hemisphere and the right column represents it for the southern hemisphere. In the upper (lower) row, background vorticity is increasing poleward (equatorward).

formulation, it is assumed that \mathbf{u}_β is well represented by $\mathbf{u}_g(x=0, y=0)$, where the coordinates $(x=0, y=0)$ represent the center of the cyclone in the moving grid.

For the numerical simulation, we use the Dedalus code package²⁷. Eq. 8 in a β -plane, is scaled according to

$$(x, y) = R(\hat{x}, \hat{y}), \quad t = \frac{R}{V}\hat{t}, \quad (9)$$

$$\mathbf{u} = V\hat{\mathbf{u}}, \quad \xi = \frac{V}{R}\hat{\xi}, \quad f = f_0 + \beta R\hat{y},$$

where V is the maximum velocity in the vortex, R is the radius of maximum velocity in the vortex, and β is the linear slope of the background vorticity. With this scaling, together with a numerical viscosity term and a Newton relaxation sponge term (F), Eq. 8 becomes (removing the hat signs for clarity)

$$\frac{\partial \xi_g}{\partial t} + (\mathbf{u}_v + \mathbf{u}_g) \cdot \nabla (\xi_g + \hat{\beta}y) + (\mathbf{u}_g - \mathbf{u}_\beta) \cdot \nabla \xi_v = \frac{1}{\text{Re}} \nabla^2 \xi_g + F, \quad (10)$$

where

$$\hat{\beta} = \frac{R^2 \beta}{V}, \quad (11)$$

and Re is a Reynolds number determining the strength of viscosity. The trap, F , is aimed to relax the relative vorticity to zero far away from the vortex, so as to avoid numerical boundary effects. Here, we define F as

$$F = -\frac{1}{2} \frac{\xi_g}{\tau_{\text{trap}}} (1 - \tanh(A(r_{\text{trap}} - r))), \quad (12)$$

where τ_{trap} defines the relaxation time scale, $r = \frac{1}{R}\sqrt{x^2 + y^2}$ is a scaled distance from the center of the cyclone, and r_{trap} is the value of r from which the relaxation begins, using a step function with a tanh form and a sharpness amplitude A . The reasoning by which Eq. 1 in the main text represents the leading order of Eq. 10 comes from assuming $\mathbf{u}_g \ll \mathbf{u}_v$, which is well supported in the model run (Fig. 2a-d), so that in the domain (far from the trap effect), we have

$$\frac{\partial \xi_g}{\partial t} + \mathbf{u}_v \cdot \nabla (\xi_g + \hat{\beta}y) + (\mathbf{u}_g - \mathbf{u}_\beta) \cdot \nabla \xi_v \approx 0, \quad (13)$$

where $\text{Re}^{-1} \ll 1$. The reason why $\mathbf{u}_v \cdot \nabla (\xi_g + \hat{\beta}y) \gg (\mathbf{u}_g - \mathbf{u}_\beta) \cdot \nabla \xi_v$ is harder to justify and is discussed in depth by Ref. ¹³. Here, we suffice noting that at the beginning of the motion, $(\mathbf{u}_g - \mathbf{u}_\beta)$ is almost zero, but also later, at the core area where $\nabla \xi_v$ is significant, $\mathbf{u}_g \approx \mathbf{u}_\beta$ so that $(\mathbf{u}_g - \mathbf{u}_\beta)$ is very small.

Model run definitions

The actual equations supplied to the model solve one variable, ψ_g , the generated streamfunction, in the form

$$\frac{\partial}{\partial t} (\nabla^2 \psi_g) + (\mathbf{u}_v + \mathbf{u}_g) \cdot \nabla (\nabla^2 \psi_g + \hat{\beta}y) + (\mathbf{u}_g - \mathbf{u}_\beta) \cdot \nabla \xi_v + \tau = \frac{1}{\text{Re}} \nabla^4 \psi_g - \frac{1}{2} \frac{\nabla^2 \psi_g}{\tau_{\text{trap}}} (1 - A \tanh(r_{\text{trap}} - r)), \quad (14)$$

where the relation between vorticity and streamfunction, $\xi_g = \nabla^2 \psi_g$, is used. The velocities in the (x, y) directions are $(u_g, v_g) = \left(-\frac{\partial \psi_g}{\partial y}, \frac{\partial \psi_g}{\partial x}\right)$. τ is a tau term required for solution in the spectral methods used by Dedalus (see Ref. ²⁷), which also require a gauge equation,

$$\iint \psi_g dx dy = 0, \quad (15)$$

over the domain. The scaled prescribed vortex profile used for the model (suggested by Ref. ³⁵, with $b = 1$) is

$$U_v = r \exp(1 - r), \quad (16)$$

where U_v is a the tangential velocity of the vortex. This profile translates into the (x, y) velocity components

$$\begin{aligned} u_v &= -U_v \sin\left(\tan^{-1}\left(\frac{y}{x}\right)\right), \text{ and} \\ v_v &= U_v \cos\left(\tan^{-1}\left(\frac{y}{x}\right)\right), \end{aligned} \quad (17)$$

respectively. Subsequently, the vortex vorticity, calculated as $\xi_v = \frac{1}{r} \frac{\partial}{\partial r} (r U_v)$, is

$$\xi_v = (2 - r) \exp(1 - r). \quad (18)$$

The equations are solved with a Fourier spectral base, implying double periodic boundary conditions. These conditions are not important in the solution due to the sponge term, forcing the vorticity field to become zero away from the center.

Model details for Fig. 2a-c In this run, we solve the equations described in this section with a resolution of 1024×1024 , in a domain with unit-less size 18×18 . The numbers for this simulation are: $\text{Re} = 1000$, $r_{\text{trap}} = 16$, $\tau_{\text{trap}} = 0.1$ $A = 20$.

Model details for Fig. 2f Here, a set of simulations are conducted to test how changes in $\hat{\beta}$ lead to changes in the time evolution of \mathbf{u}_β . The simulations run with a grid resolution of 512×512 and a unit-less domain size of 40×40 . The numbers for all of the set's simulations are: $\text{Re} = 400$, $r_{\text{trap}} = 38$, $\tau_{\text{trap}} = 0.1$ $A = 20$. The $\hat{\beta}$ values for the different runs are $\{0.0001, 0.001, 0.003, 0.005, 0.01, 0.05, 0.1\}$.

C Derivation of an idealized ‘‘center of mass’’ for shielded cyclones

In this section, a derivation is performed for finding the analog of ‘‘mass’’ for a cyclone in a multiple cyclones system. We only consider here shielded cyclones, i.e., cyclones with a ring of anticyclonic vorticity around them. In this shielded case, the interactions between cyclones are determined by the effect of the vorticity gradient of one cyclone on another ^{19,24}, rather than the advective interactions of one cyclone's tangential velocity on another. Indeed, the polar cyclones of Jupiter are suspected to be shielded based on observations ¹⁹ and on stability in shallow-water model simulations ²³.

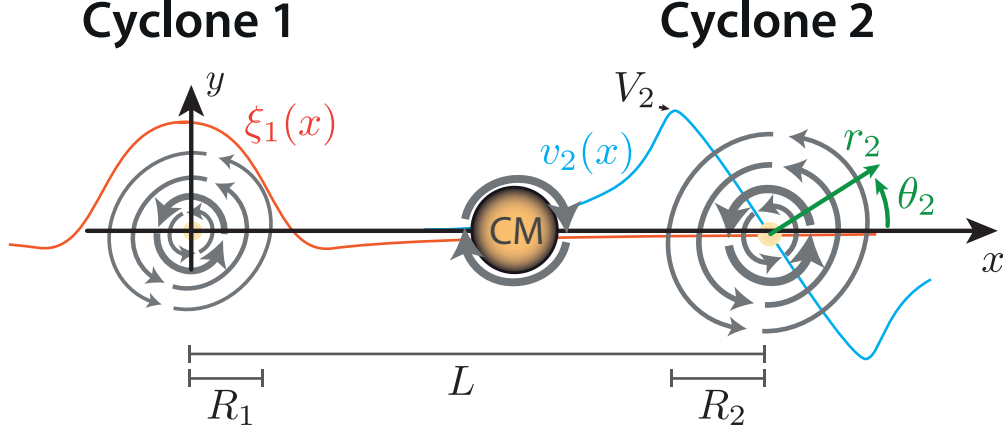


Figure S2: An illustration of the geometry for deriving a “center of mass” between 2 cyclones.

For this derivation, we consider the interaction between two interacting cyclones (Fig. S2). The instantaneous vorticity gradient force (put here in terms of averaged acceleration) of Cyclone 1 on Cyclone 2 in the x direction can be shown¹⁹ to be proportional to

$$\pi R_2^2 \frac{\partial \overline{u_{\beta,2}}}{\partial t} \approx \iint \xi_1 v_2 dS, \quad (19)$$

where R_i is the cyclone’s radius of maximum velocity, $\overline{u_{\beta,i}}$ is the mean, over the cyclone’s core, drift velocity (by the vorticity gradient forces) in the x direction, ξ_i is the vorticity profile of a cyclone, v_i is the y component of a cyclone’s tangential velocity, dS is the integration area over the cyclone’s core, and i is the index of the cyclone (1 or 2 for this derivation). The dimensional forms of Eqs. 16-18 for a cyclone’s velocity and vorticity profiles are

$$v_i = V_i \frac{r_i}{R_i} \exp\left(1 - \frac{r_i}{R_i}\right) \cos(\theta_i), \quad (20)$$

$$\xi_i = \frac{V_i}{R_i} \left(2 - \frac{r_i}{R_i}\right) \exp\left(1 - \frac{r_i}{R_i}\right), \quad (21)$$

where r_i and θ_i represent the polar coordinates relative to cyclone i , and V_i is the maximum velocity of the cyclone. A series expansion of ξ_1 around the center of Cyclone 2 ($r_1 \rightarrow \sqrt{(L + r_2 \cos \theta_2)^2 + (r_2 \sin \theta_2)^2}$, where L is the distance between the cyclones) gives

$$\xi_1 \approx \frac{V_1}{R_1^3} \exp\left(1 - \frac{L}{R_1}\right) (R_1 (2R_1 - L) + r_2 \cos \theta_2 (L - 3R_1)), \quad (22)$$

or, assuming $L \gg R_1$,

$$\xi_1 \approx \frac{V_1 L}{R_1^3} \exp\left(1 - \frac{L}{R_1}\right) (r_2 \cos \theta_2 - R_1). \quad (23)$$

Similarly expanding v_2 around $r_2 \rightarrow 0$, we get

$$v_2 = V_2 \frac{r_2}{R_2} \exp\left(1 - \frac{r_2}{R_2}\right) \cos(\theta_2). \quad (24)$$

Plugging the expansions in Eq. 19, after performing the integration ($dS = r_2 dr_2 d\theta_2$ in the boundaries $\{0 \leq r_2 \leq R_2\}$ and $\{0 \leq \theta_2 \leq 2\pi\}$) gives

$$\frac{\partial \overline{u_{\beta,2}}}{\partial t} \approx \exp\left(2 - \frac{L}{R_1}\right) \frac{LR_2 V_1 V_2}{4R_1^3}. \quad (25)$$

Similarly, for Cyclone 1

$$\frac{\partial \overline{u_{\beta,1}}}{\partial t} \approx -\exp\left(2 - \frac{L}{R_2}\right) \frac{LR_1 V_1 V_2}{4R_2^3}. \quad (26)$$

Multiplying Eq. 25 by $\frac{1}{R_2^4} \exp\left(-\frac{L}{R_2}\right)$ and Eq. 26 by $\frac{1}{R_1^4} \exp\left(-\frac{L}{R_1}\right)$ we get

$$\exp\left(-\frac{L}{R_2}\right) \frac{1}{R_2^4} \frac{\partial \overline{u_{\beta,2}}}{\partial t} \approx \exp\left(2 - \frac{L}{R_1} - \frac{L}{R_2}\right) \frac{LV_1V_2}{4R_1^3R_2^3}, \quad (27)$$

$$\exp\left(-\frac{L}{R_1}\right) \frac{1}{R_1^4} \frac{\partial \overline{u_{\beta,1}}}{\partial t} \approx -\exp\left(2 - \frac{L}{R_1} - \frac{L}{R_2}\right) \frac{LV_1V_2}{4R_1^3R_2^3}. \quad (28)$$

Thus, summing Eqs. 27 and 28 gives

$$\exp\left(-\frac{L}{R_2}\right) \frac{1}{R_2^4} \frac{\partial \overline{u_{\beta,2}}}{\partial t} + \exp\left(-\frac{L}{R_1}\right) \frac{1}{R_1^4} \frac{\partial \overline{u_{\beta,1}}}{\partial t} = 0, \quad (29)$$

representing the ‘‘center of mass’’ between the cyclones that does not feel any acceleration in this simplified case. Finally, we propose that for a group of cyclones, the ‘‘center of mass’’ analogy of ‘‘mass’’ gets the form

$$m_i = \frac{\exp\left(-\frac{L}{R_i}\right)}{R_i^4}, \quad (30)$$

where L represents an estimate for the average distance between cyclones in the group.

D Simulations for the motion of a group of cyclones compared to one equivalent cyclone

In this section the model formulation resulting in Fig. 3 is presented. These simulations were also conducted with the Dedalus package²⁷. For these results we are simply solving the barotropic vorticity equation (Eq. 5) scaled according to Eq. 9, leading to

$$\frac{\partial}{\partial t} (\nabla^2 \psi) + \mathbf{u} \cdot \nabla \left(\nabla^2 \psi + \frac{1}{2} \hat{\beta} y (1 - \tanh(A(r_{\text{trap}} - r))) \right) + \tau = \frac{1}{\text{Re}} \nabla^4 \psi. \quad (31)$$

Here, the f term is multiplied by a trap function such that a discontinuity in f traps vorticity anomalies (similar to Ref.²⁹). In this model we conduct two simulations. In the first run, a group of 6 cyclones are inserted in the initial conditions of ψ according to

$$\xi_i = \left(2 - r_i^b\right) \exp\left[\frac{1}{b} \left(1 - r_i^b\right)\right], \quad (32)$$

where i represents the index of the cyclone (from 1 to 6), r_i is defined by

$$r_i = \sqrt{(x - x_i)^2 + (y - y_i)^2}, \quad (33)$$

and (x_i, y_i) are the initial coordinates of the center of cyclone i . The initial (dimensional) locations of the 6 cyclones were $\{(19.998, -14.000), (15.854, -8.295), (9.147, -10.474), (9.147, -17.526), (15.854, -19.705), (14.000, -14.000)\} \times 10^3$ km. For Fig. 3a-c, the cyclones all have $R = 1000$ km, $V = 80 \text{ ms}^{-1}$ and $b = 0.78$. In the simulation for the equivalent cyclone, only one such cyclone was planted in the initial conditions at the location $(14.000, -14.000) \times 10^3$ km. The initial condition for ψ (ψ_0) was solved from the Poisson equation,

$$\nabla^2 \psi_0 = \xi_0, \quad (34)$$

where $\xi_0 = \sum_i \xi_i$. These simulations had a grid resolution of 1024×1024 and a domain size of $(37.36 \times 37.36) \times 10^3$ km. The numbers

for these simulations are: $\text{Re} = 8 \times 10^9$, $r_{\text{trap}} = 37.095 \times 10^3$ km, $A = 20$, $\hat{\beta} = 7 \times 10^{-3}$. The trajectories of the cyclones shown in Fig. 3 were produced by searching the local maxima of vorticity in each vorticity snapshot, using the *maximum_filter* function of the *scipy* package in Python. As the initial cyclones are identical, the CM trajectory is calculated simply as an average of the (x, y) coordinates of all the cyclones per snapshot.

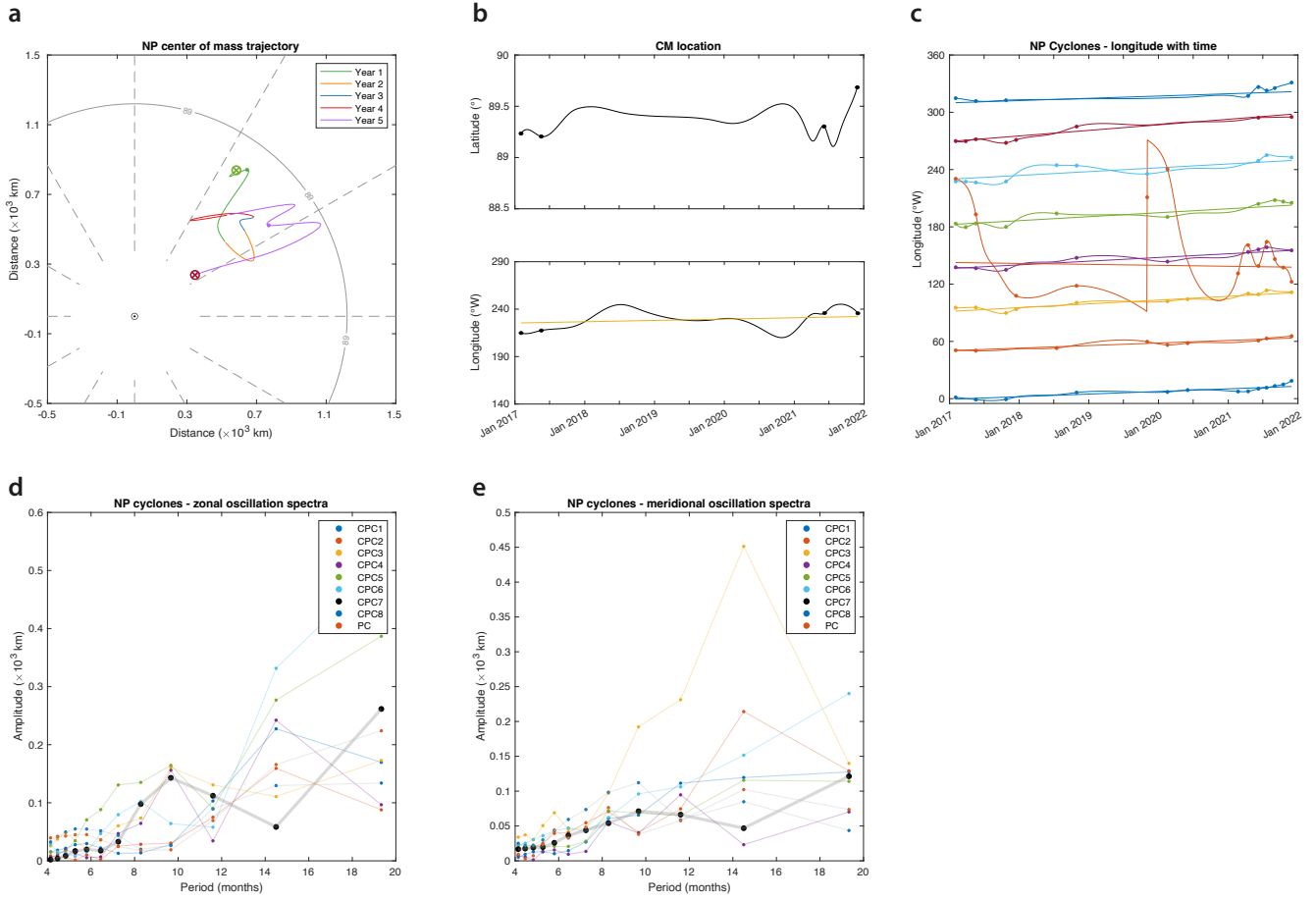


Figure S3: The same as Fig. 4 in the main text but for the north pole. As the data is very infrequent, only the motion exhibited by the moving average (Fig. 1f of the main text) has a significance for the analysis of this study.

Simulations with size variance

To more generally test the CM analogy, simulations with variance in the cyclones' sizes are conducted. In one experiment (Fig. 3d), the 6-cyclone simulation has $R = 1000$ km, $V = 80$ ms⁻¹ and $b = 0.78$, except one cyclone that has $R = 500$ km. In another case (Fig. 3e), a second cyclone is also set to $R = 500$ km, and a third cyclone is set to $R = 1200$ km. The initial locations of the 6 cyclones are the same as in the 6 identical cyclones case. The orange line, representing the CM motion is calculated according to Eq. 30, where L is estimated as 6×10^3 km. For the equivalent cyclone run, the starting location is according to the starting position of the CM in each case. The characteristics of the equivalent cyclone are determined as a “mass”-weighted (using Eq. 30) average of the characteristics of the 6 cyclones. There may be a more straightforward way to estimate the characteristics of the equivalent cyclone to be derived in future studies. In these simulation cases (Fig. 3d-e), the motion of each cyclone is completely different than the motion in the results of Fig. 3a, but the CM motion is still highly correlated with the motion of the equivalent cyclone.

E Center of mass calculations from the observations

For Fig. 4a-e we only use data from the south pole, as the data from the north pole is too infrequent for a meaningful analysis (See SI Fig. S3). For Fig. 4c we translate back the interpolated trajectories into polar coordinates according to

$$\theta = \cos^{-1} \left(\frac{\sqrt{x^2 + y^2}}{R_J} \right), \quad \lambda = \tan^{-1} \left(\frac{y}{x} \right) - \frac{\pi}{2}. \quad (35)$$

The straight lines in Fig. 4c are linear regression lines. To plot the spectra (Fig. 4d-e) we calculated, for each cyclone, the cumulative zonal (l_λ) and meridional (l_θ) distances per time step (i) according to

$$\begin{aligned} l_\lambda^i &= l_\lambda^{i-1} + R_J \cos(\theta^i) (\lambda^i - \lambda^{i-1}), \\ l_\theta^i &= l_\theta^{i-1} + R_J \cos(\theta^i - \theta^{i-1}), \end{aligned} \quad (36)$$

where $l_\lambda^0 = l_\theta^0 = 0$. Then, after the mean and linear trends are removed, a fast Fourier transform (FFT) was performed on the time series defined by Eq. 36. This procedure produces the amplitudes (in length units) per oscillation period for each cyclone. Due to the long period of the collected data, which is on the order of 50 days (~ 53 days until PJ 34 and ~ 43 days after), only oscillation amplitudes with periods larger than 4 months are displayed. Also, we only show oscillations with periods up to 20 months, as oscillations with larger periods have less than 3 repetitions in the total available data, containing ~ 5 years.

For the calculation of the CM, the different cyclones are weighted according to m_i (Eq. 30), such that the CM coordinates at each observation time are

$$(x_{\text{CM}}, y_{\text{CM}}) = \left(\frac{\sum x_i m_i}{\sum m_i}, \frac{\sum y_i m_i}{\sum m_i} \right), \quad (37)$$

where i is the index of the cyclone (1–9 in the north pole and 1–6 in the south) and L is assumed to be 6,000 km, in agreement with observational estimates (see the next section for the sensitivity of the analysis to this choice). For R_i , we use the data from Ref. 6, which gives estimations of the sizes for the cyclones in the north and south poles based on Juno observations. As R_i is the radius of maximum velocity, we use the best fit from Ref. 1 for the velocity fields of the PCs during PJ4⁸ of 770 km and 970 km for the north and south PCs, respectively. The respective sizes of the PCs in Ref. 6 at PJ4, representing a total size rather than size of maximum velocity, are 4440 km and 6930 km for the north and south, respectively. Thus, to use the data of Ref. 6, the cyclone sizes are averaged over PJs, and normalized by $770/4440$ in the north and by $970/6930$ in the south. The resulting R_i are presented in Tab. S1. For calculating $\hat{\beta}$ (Eq. 11), the maximum velocities of the cyclones are required, but there is no published data at the moment. We therefore use the values estimated only for the PCs of $V_i = 90$ and 95 ms^{-1} for the cyclones in the north and south poles, respectively¹. Such variability, however, is less significant for the determination of $\hat{\beta}$ relative to the squared R_i variability.

Determining β for the cyclones is more nuanced. In the β -plane case (Fig. 3), β is trivial since it is constant for all cyclones at all times. In the polar case, however, different latitudes have different values of β . In addition to that, while the direction of β is constant in the polar coordinates, the hydrodynamics happen in the Cartesian coordinates, where β changes direction relative to the pole. Thus, to evaluate the drifts (i.e., evaluate Eq. 11) we set β as equal between the cyclones at each pole according to a temporal average of the vector sum of the directional β of each cyclone at each PJ for which we have a size estimation. Specifically, for each PJ where we have location and size data for the cyclones (only two such PJs in the north pole), we calculate for each pole

$$\beta_{\text{PJ } j} = \frac{1}{\sum_{\text{cyc } i} m_{ij}} \left| \sum_{\text{cyc } i} \vec{\beta}_{ij} m_{ij} \right|, \quad (38)$$

which is a “mass” weighted vector sum of the directional beta

$$\vec{\beta}_{ij} = -\frac{2\Omega}{R_J} \cos(\theta_{ij}) \frac{\mathbf{r}_{ij}}{|\mathbf{r}_{ij}|}, \quad (39)$$

that has the magnitude of β and a direction pointing towards the pole (θ_{ij} and \mathbf{r}_{ij} are the latitude and location vector relative to the pole of cyclone i at PJ j , respectively). Jupiter’s rotation rate is set as $\Omega = 1.7585 \times 10^{-4} \text{ s}^{-1}$. Lastly, the value we use for β for each pole is set as

$$\beta = \frac{1}{n} \sum \beta_{\text{PJ } j} \quad (40)$$

over the n PJ with sufficient data. This calculation leads to $\beta = \{4.862, 8.896\} \times 10^{-14} (\text{ms})^{-1}$ for the north and south poles, respectively. The CM value of $\hat{\beta}$ for each pole is calculated by

$$\hat{\beta}_{\text{CM}} = \frac{\sum R_i^2 m_i \beta}{\sum m_i V}, \quad (41)$$

which gives the values $\hat{\beta}_{\text{CM}} = \{3.771, 7.257\} \times 10^{-4}$ for the north and south poles, respectively.

The zonal velocities of the individual cyclones are calculated in units of longitude ($^\circ$) per year and in metric units. For the longitude case, the velocities were calculated from a linear fit over the observed longitudes (Fig. 4c). For the metric case, first the zonal cumulative distance (l_λ) was calculated for each cyclone track according to Eq. 36, on which a linear fit was conducted for the mean velocity. The results of both forms are laid out in Tab. S2. As discussed in the main text, two forms are presented for the zonal

	PC	CPC1	CPC2	CPC3	CPC4	CPC5	CPC6	CPC7	CPC8	Mean
North pole R_i (km)	969	789	757	771	732	891	823	810	756	811
North pole $m_i/\Sigma m_i$	18.26%	10.01%	8.65%	9.26%	7.54%	14.83%	11.67%	11.08%	8.61%	
South pole R_i (km)	875	847	963	927	769	782	-	-	-	861
South pole $m_i/\Sigma m_i$	17.57%	15.95%	22.40%	20.48%	11.42%	12.18%	-	-	-	

Table S1: An estimation for the cyclone sizes, and their relative weight, according to the data from Ref. ⁶.

	PC	CPC1	CPC2	CPC3	CPC4	CPC5	CPC6	CPC7	CPC8	CM1	CM2
North pole u_i (cm s ⁻¹)	-1.10	1.52	1.42	2.22	2.24	2.51	2.19	3.49	0.99	1.55	0.23
North pole u_i (°/year)	-6.71	2.89	2.85	4.07	4.28	4.96	5.00	5.70	2.78	2.20	4.04
South pole u_i (cm s ⁻¹)	2.95	4.39	3.43	3.42	4.37	4.39	-	-	-	3.72	3.47
South pole u_i (°/year)	9.24	7.83	7.69	7.74	9.05	7.86	-	-	-	8.17	4.85

Table S2: An estimation for the cyclone westward-drift velocities.

velocity of the CM. For CM1 (Fig. 4f), the velocity is calculated as the weighted average of u_i (the zonal velocities of the individual cyclones, Tab. S2) according to

$$u_{\text{CM1}} = \frac{\sum u_i m_i}{\sum m_i}. \quad (42)$$

For CM2, the velocities are calculated from the trajectory of the CM by Eq. 36, where the latitude and longitude are those of the CM and u_{CM2} results from finally doing a linear fit on l_{λ}^{CM} for the upper panel of Fig. 4f. For the lower panel of Fig. 4f, the velocities result from a linear fit of the CM's longitude time series (lower panel of Fig. 4b).

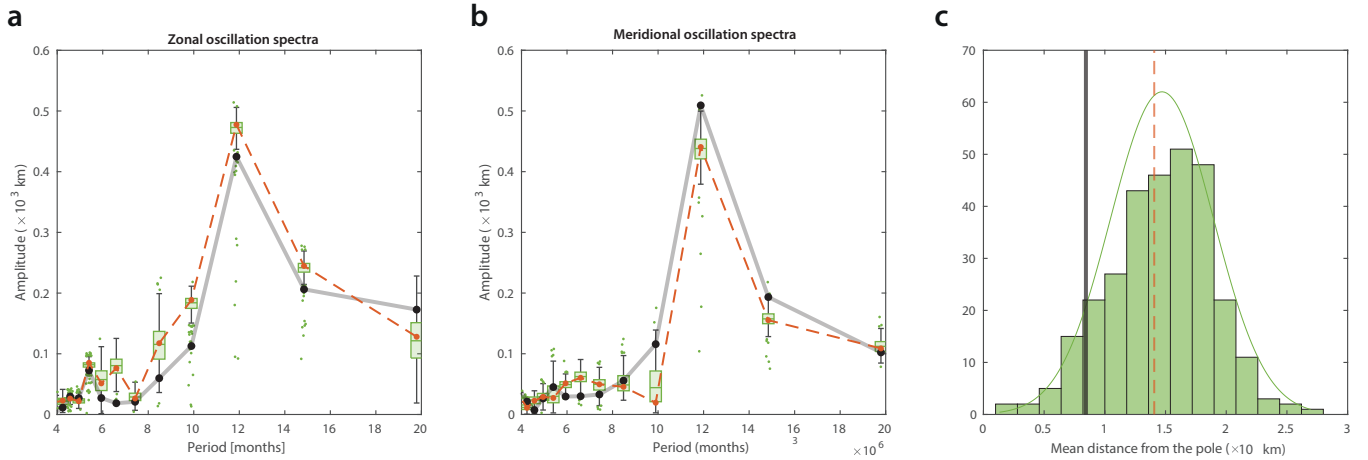


Figure S4: A sensitivity analysis of the CM in Jupiter's south pole to the cyclones' parameters. (a and b) The oscillation spectra in the zonal (a) and meridional (b) directions of the CM. The black curves represent a CM trajectory weighted with the observational estimation of the cyclones' sizes (Tab. S1), which is the same as the black curves in Fig. 4d-e. The orange dashed curves represent a CM trajectory calculated with all cyclones weighted equally, such that it represents a geometric mean. The green box plots are a statistical representation of 300 randomly generated sets of weights (see text), where the box is defined by the upper and lower quantiles (with the median being the line inside the box), the black "whiskers" are the maximum and minimum values that are not outliers (where outliers are values away from the box boundaries by 1.5 times the size of the box), and the green dots are outliers. (c) A histogram showing the amount of randomly generated sets (ordinate) that corresponds with each range of calculated R_{mean} (see text). Here the green curve represents a normal distribution of the random sets, the black line is calculated using the observational estimated weights, and the orange dashed line is calculated using equally weighted cyclones.

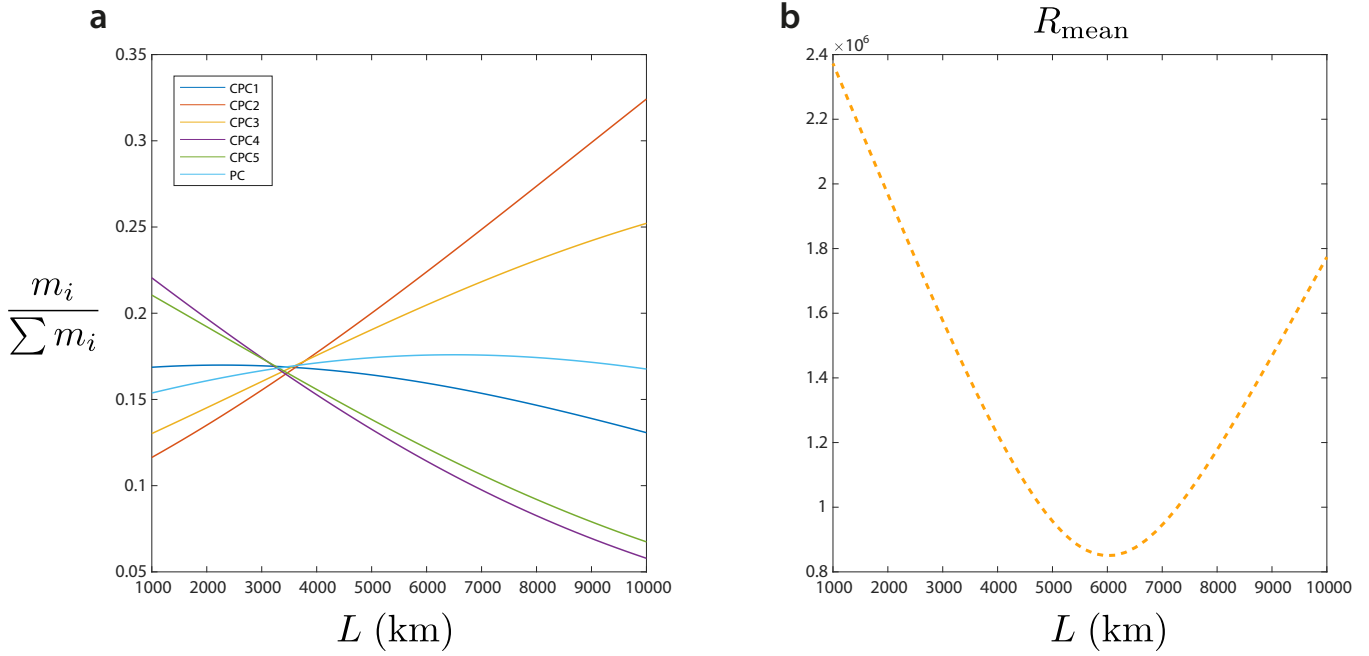


Figure S5: Sensitivity of m_i (a) and the mean distance of the CM from the pole (b) to the choice of L . This figure is only for the south pole.

Sensitivity of the results to the cyclones' weights

The following section serves to answer two questions: *i*) what is the sensitivity of the analyses of Fig. 4 to the “mass” of each cyclone? *ii*) How adequate is the estimation of m_i (Eq. 30) determined in this study, when viewed through the lens of the analyses of Fig. 4 of the main text? To answer these, we compare the Tab. S1 values against random sets of values and against a “geometric mean” set, where each cyclone is weighted equally. Each random set is constructed by assigning to each cyclone a random R_i from a student's t-distribution (Matlab's `trnd()` function) with the mean and variance of the third row of Tab. S1, and a sample size of 6. This way the cyclones retain a distribution of sizes similar to the one estimated from the observations. The weight of each cyclone is then calculated, as before, by $m_i/\sum m_i$.

For Fig. S4, 300 such random sets are generated. In Fig. S4a-b the oscillation spectra (zonal in a, and meridional in b) of the CM, calculated using these random sets for the weights, are presented in the form of box plots (in green). It can be seen that while the meridional spectra of the random sets is relatively similar to the observational weighted set, in the zonal spectra, using the observational values significantly reduces the small period oscillations (periods of 6-10 months), and thus the observational values better represent the “real” CM, which should ideally only retain the one oscillation mode (~12 months), forced only by the planetary PV gradient. Another interesting aspect of Fig. S4a-b, which supports our determination of the cyclones' weights, is that for the orbital mode (~12 months), the black curve has a higher amplitude in the meridional direction and a lower amplitude in the zonal direction than the majority of the random sets. This signifies an elliptical orbit with a semi-major axis in the meridional direction for the black case, similar to what we would expect from an ideal representation of a CM for this motion, with a radial force in the poleward direction (Fig. 3f). In Fig. S4c, the mean distance of the CM's trajectory,

$$R_{\text{mean}} = \sqrt{\left(\frac{1}{n} \sum_{i=1}^n x_{\text{CM},i}\right)^2 + \left(\frac{1}{n} \sum_{i=1}^n y_{\text{CM},i}\right)^2}, \quad (43)$$

where n is the size of the interpolated data, is calculated for each case. This parameter represents how close is the overall mean position of the trajectory to the pole, and should be as close to zero as possible for a “physical” representation of the CM (Fig. 3f). It can be seen that indeed the black line, representing the observational weights, has smaller R_{mean} than the majority of the random sets and than the equally weighted set, supporting the use of these observationally based weights to the CM analyses.

Sensitivity to the parameter L Here, we see look at the sensitivity to the parameter L , which represents a mean distance between the cyclones (Fig. S2). In Fig. S5a, we see how the weights of each cyclone in the south pole would change when changing L .

Interestingly, our choice ($L = 6,000$ km, based on an estimation from Fig. 1 of the main text) represents a minimum when considering how R_{mean} of the motion of the CM changes with L (Fig. S5b). This choice of L , is also consistent with the minimum distance between cyclones for stability (L_{lim}) that was calculated in Ref. ¹⁹, where it was calculated that $L_{\text{lim}} \approx 6R_{\text{CPC}}$ and where the cyclone's radius of maximum velocity is $R_{\text{CPC}} \approx 1,000$ km.